Key Points:
- Only Thompson aerosol-aware scheme can reproduce observed raindrop size distribution characteristics of Typhoon Matmo
- Raindrop number concentration near the freezing level produced by the autoconversion process determines the raindrop size distribution
- Adequately predicting cloud number concentration is crucial for capturing the right raindrop size distribution for landfalling typhoons

Correspondence to:
M. Wang,
mjwang@nju.edu.cn

Evaluation of Simulated Drop Size Distributions and Microphysical Processes Using Polarimetric Radar Observations for Landfalling Typhoon Matmo (2014)

Mingjun Wang[1] , **Kun Zhao[1]** , **Yujie Pan[2]** , and **Ming Xue[1,3]**

[1]Key Laboratory of Mesoscale Severe Weather/MOE and School of Atmospheric Sciences, Nanjing University, Nanjing, China, [2]Collaborative Innovation Center on Forecast and Evaluation of Meteorological Disasters/Key Laboratory of Meteorological Disaster, Ministry of Education/Joint International Research Laboratory of Climate and Environment Change, Nanjing University of Information Science and Technology, Nanjing, China, [3]Center for Analysis and Prediction of Storms and School of Meteorology, University of Oklahoma, Norman, OK, USA

Abstract The Morrison (Morr), Thompson (Thom), Thompson aerosol-aware (ThomA), and WRF double-moment 6-class (WDM6) microphysics schemes within the WRF model are used to simulate landfalling Typhoon Matmo (2014) and evaluated against polarimetric radar observations in terms of raindrop size distribution (RSD) and microphysical processes. Focus is placed on the inner rainband convection. Only ThomA is able to reproduce observed RSD characteristics having even smaller mean raindrop sizes and larger number concentrations than those of typical maritime convection, when measured in terms of mass-weighted mean diameter and normalized RSD intercept parameter. The diagnoses of microphysical transfer terms show that warm rain processes are dominant in all experiments. The accretion and autoconversion processes dominate the production of rainwater content and raindrop number concentration, respectively. Examinations of vertical profiles of hydrometeor masses and number concentrations as well as rainwater-related microphysical transfer rates suggest that raindrop total number concentration N_{Tr} near the freezing level, mainly produced by the autoconversion process, plays an important role in determining the near-surface RSD characteristics. Morr and Thom assume fixed values of cloud droplet number concentration N_{Tc} that are much larger than those predicted by ThomA, leading to much smaller N_{Tr} near the freezing level produced by the autoconversion process. Sensitivity experiments using much reduced N_{Tc} substantially increase predicted N_{Tr}, mainly through invigoration of autoconversion. These results indicate that adequately predicting N_{Tc} is very important for capturing the right RSD characteristics for landfalling typhoons over East China where Typhoon Matmo is one of the representative examples.

1. Introduction

Studies (e.g., Fovell et al., 2009; Khain et al., 2016; Pattnaik et al., 2010) have demonstrated that microphysical processes are important to accurately predicting tropical cyclones (TCs). Microphysical parameterizations (MPs) have been widely used in numerical weather prediction models to represent complex cloud microphysical and precipitation processes. Nonlinear interactions between microphysical and dynamical processes through latent heat release and absorption in microphysical processes are particularly critical for TC forecasts (Didlake & Kumjian, 2018; Feng & Bell, 2019; Igel et al., 2014). To describe the complex microphysical processes, more complicated MP schemes have been developed that include more hydrometeor species, more physical processes, and higher degrees of freedom in describing the particle size distribution (PSD) functions. Such enhancements do not necessarily lead to forecast improvements, due to the increased level of uncertainties associated with the increased complexity in both PSD treatments and microphysical processes. Therefore, it is important to objectively evaluate the representations of microphysics schemes in terms of both PSD and microphysical processes.

The impacts of MP schemes on forecasts of TCs' intensity and track have been extensively studied (e.g., Tao et al., 2011; Yang & Ching, 2005; Zhu & Zhang, 2006), although most of the existing results only infer indirectly the relative performance of different MP schemes. In situ observations can provide direct

measurements of PSDs and hydrometeor types (e.g., Black & Hallett, 2012; McFarquhar & Black, 2004; Tokay et al., 2008); however, in situ observations are quite limited in terms of spatial and temporal coverage and thus barely used to validate MP schemes. In comparison, radar reflectivity, which is defined as the summation of the sixth power of diameters from all particles within a given sampling volume, can partly provide three-dimensional (3-D) distribution of the PSD with high spatial and temporal resolutions. Studies have used radar reflectivity data to evaluate rainbands and precipitation structures of TCs simulated using different MP schemes (e.g., McFarquhar et al., 2006, 2012; Rogers et al., 2007). Results have shown that model simulated reflectivity is generally higher than the observation, but the cause of such overestimation cannot be identified just using the limited information from the reflectivity observations.

Polarimetric radars, transmitting horizontal and vertical polarized electromagnetic waves, allow us to derive several polarimetric variables containing more microphysical information, in addition to the reflectivity factor of horizontal polarization (Z_H). These variables include differential reflectivity (Z_{DR}), differential propagation phase shift (ϕ_{DP}), specific differential phase (K_{DP}), and copolar correlation coefficient (CC) (Bringi & Chandrasekar, 2001), and they are related to the size, shape, orientation, and water phase of the hydrometeors (Bringi & Chandrasekar, 2001; Doviak & Zrnić, 2006). The PSD and hydrometeor types can be further retrieved/identified through objective techniques (e.g., Park et al., 2009; Vivekanandan et al., 1999; Zhang et al., 2001), which can reveal more information about the microphysical characteristics and dominant microphysical processes. More descriptions of polarimetric radar variables can be found in Bringi and Chandrasekar (2001).

Benefiting from their microphysical information content and large spatial coverage, polarimetric radar data have recently been used to validate simulated mesoscale convective systems (Barnes & Houze, 2016; Putnam et al., 2017), Changma frontal precipitation (Johnson et al., 2018), supercell storms (Johnson et al., 2016, 2018; Snyder et al., 2017a, 2017b), and TCs from different MP schemes in numerical model (Brown et al., 2016, 2017). Brown et al. (2016) tested six different MP schemes available in the Advanced Research Weather Research and Forecasting model (WRF) (Skamarock et al., 2005) for two landfalling hurricane cases. Results showed that most of the MP schemes simulated higher Z_{DR} values than the observation, among which the Thompson aerosol-aware bulk scheme and spectral bin scheme had the best agreement with the observations. Brown et al. (2017) further extended the investigation of the Thompson aerosol-aware scheme, and found that a larger median raindrop size than the observation mainly occurred in regions of light stratiform precipitation. A modification to the scheme by increasing the number production of rain drops from melting snow was shown to improve the simulated raindrop size distribution (RSD). The studies of Brown et al. (2016, 2017) mainly evaluated the ability of MP schemes in reproducing the RSD characteristics in landfalling hurricanes, but validations of microphysical processes were little discussed. Also, the key processes leading to the substantial differences among MP schemes would require careful investigations.

To better understand microphysical processes, Wang, Zhao, et al. (2016, 2018) applied polarimetric radar data to landfalling Typhoon Matmo (2014) and examined the microphysical characteristics and dominant processes. Polarimetric radar and two-dimensional video disdrometer (2DVD) observations indicated that the convection of the inner rainband of Matmo was generally consisted of smaller drops and higher number concentrations than the typical maritime type convection (Wang, Zhao, et al., 2016). The 2DVD observations from seven typhoons after making landfall in China further confirmed that this is a common microphysical characteristic of landfalling typhoon precipitation over China (Wen et al., 2018). Results also suggested that the rain water production in convective regions was mainly achieved through warm-rain processes. Wang et al. (2018) further investigated the vertical variations of Z_H, Z_{DR}, and rain water content, and found that heavy rainfall primarily formed through warm-rain processes and graupel particle melting. The warm-rain precipitation was initiated with raindrops generated through the autoconversion process immediately below the freezing level, and then the rain water content mainly grew through accretion process, while the coalescence process was dominant below 2 km.

It is worth examining if MP schemes in numerical models can reproduce the quite unique observed RSD characteristics and dominant rain form processes within landfalling typhoons over China. In this study, Typhoon Matmo (2014) is simulated using four different bulk MP schemes in the WRF model and the results are verified against observations collected by a polarimetric radar and a 2DVD. The simulated RSDs are
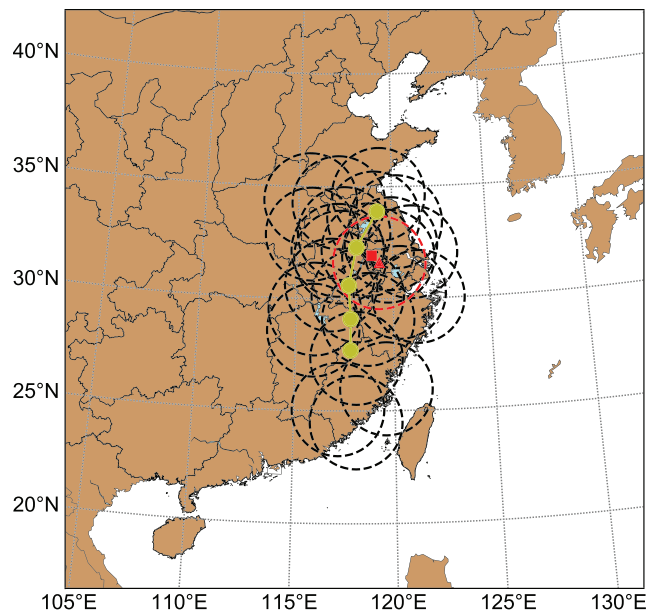
Figure 1. The physical domain of the numerical simulation, with the best track locations (marked by yellow dots) plotted every 6 hr from 0000 UTC 24 to 0000 UTC 25 July 2014 from China Meteorological Administration (CMA). The dashed circles denote the radial velocity coverage of 230 km of operational radar stations. The red circle indicates the coverage of LSRD.

carefully validated by using a polarimetric radar data simulator (PRDS), and the simulated microphysical processes are examined through raindrop mass and concentration source/sink diagnoses. Moreover, sensitivity tests are conducted to identify the key factors leading to the unique RSD characteristics. As in our previous studies, this study again focuses on the inner rainband convection on which observational data are available.

The rest of the paper is organized as follows. Section 2 describes observations, the WRF model configurations, and analysis methods used in this study. The evaluations of simulated PSD signatures are presented in section 3. Section 4 examines the microphysical differences between MP schemes and investigates the key factor producing the unique PSD characteristics. Section 5 presents the sensitivity tests that further demonstrate the key factor responsible for the observed RSD characteristics. Conclusions and discussions are given in section 6.

2. Methods and Experimental Design

2.1. Data for Verification

To evaluate the performances of MP schemes, the same data sets employed in Wang, Zhao, et al. (2016) are used in this study, including data collected by an S-band polarimetric radar located at Lishui (marked as LSRD), a radiosound, and a 2DVD located in Nanjing (Figure 1). All data were carefully processed. The time span of the radar data is from 0600 to 1600 UTC 24 July 2014, covering the whole lifecycle of the inner rainband as it moved across the radar coverage area. As in Wang, Zhao, et al. (2016), the constrained gamma RSD model (Zhang et al., 2001) is used to retrieve the RSD from the polarimetric radar data. Considering the observation errors of polarimetric variables, RSDs are not retrieved when Z_{DR} is less than 0.1 dB, corresponding to the minimum mass-weighted mean diameter of ~0.9 mm.

2.2. WRF Model and MP Schemes

This study tests four bulk MP schemes available in the WRF model (Skamarock et al., 2005) version 3.9. The model domain is 720×720 grid points and has a 4 km horizontal grid spacing (Figure 1). Fifty vertical levels are unevenly distributed between the surface and the model top of 50 hPa with maximum resolution near the surface. All simulations used the following physics parameterizations: the Noah land-surface model (Ek et al., 2003), the Yonsei University boundary layer scheme (Hong et al., 2006), RRTMG longwave and shortwave radiation schemes (Iacono et al., 2008). The NCEP Global Forecast System (GFS) analyses at 0.5° resolution are used to create the initial and boundary conditions.

The four MP schemes examined are the Morrison double-moment scheme (Morrison scheme; Morrison et al., 2005) without coupling with WRF-Chem, the regular Thompson scheme (Thompson et al., 2008), the Thompson aerosol-aware scheme (Thompson & Eidhammer, 2014), and the WRF double-moment 6-class scheme (WDM6 scheme; Lim & Hong, 2010). All the MP schemes predict mass mixing ratios of cloud water, ice, rain, snow, and graupel. For liquid species, all MP schemes predict the number concentration of rain, and only the Thompson aerosol-aware scheme and WDM6 scheme predict the number concentration of cloud droplets. Instead of predicting the number concentration of cloud droplets, prescribed values of cloud droplet total number concentrations of 2.5×10^8 and 10^8 m^{-3} are used in the Morrison scheme and the Thompson scheme, respectively. Based on Brown et al. (2017), the snow melt exponential constant for the regular and aerosol-aware Thompson schemes in WRF version 3.9 has been set to -0.25.

2.3. EnKF Data Assimilation

To ensure the consistency of wind fields among the different MP schemes, radial velocity observations from 25 Chinese Meteorological Administration (CMA) operational Doppler radars are assimilated into the model using the ensemble Kalman filter (EnKF) in the Advanced Regional Prediction System (ARPS) (Jung et al., 2008; Tong & Xue, 2005). An initial 40-member ensemble is created by adding perturbations to the GFS analysis at 1800 UTC 23 July 2014. The initial ensemble perturbations are generated using the cv3 background

error covariance option within the WRF's 3-D variational data assimilation package (Barker et al., 2004). Horizontal wind components, potential temperature, and mixing ratio for water vapor are perturbed, and their error statistics are defined by the climatological background error covariance. The perturbations are added to the GFS analysis to start the initial ensemble, which is first integrated for 6 hr to develop reasonable flow-dependent covariance structures before assimilating the first observation. The boundary conditions are perturbed in the same manner as the initial ensemble.

After the 6-hr ensemble forecasts, radial velocity observations are assimilated every 30 min from 0000 to 1800 UTC 24 July 2014. Covariance localization radii of 10 km in the horizontal and 4 km in the vertical are chosen when assimilating radial velocity data. A posterior relaxation-to-prior adaptive covariance inflation (Whitaker & Hamill, 2012) with $\alpha = 0.9$ is applied at those model grid points directly affected by observations to help maintain the ensemble spread. Localization and inflation parameters are chosen based on the experience obtained from Wang et al. (2014; Wang, Xue, et al., 2016) and a set of sensitivity experiments. The EnKF only updates zonal and meridional winds to constrain the kinematic structure while allowing the model microphysics physics to freely evolve throughout the data assimilation cycles. Similar procedure has been used in Barnes and Houze (2016) to force simulations to have similar dynamical evolution with impacts on microphysical processes as little as possible. Four simulations, differing only the MP schemes used, are then conducted (Table 1). The 30-min deterministic forecasts starting from ensemble mean analyses, during the period of 0600 to 1800 UTC, after radial velocity data have been assimilated for 6 hr, are used for further analyses.

2.4. Polarimetric Simulator

The PRDS developed by the Center for Analysis and Prediction of Storms (Dawson et al., 2014; Jung et al., 2008, 2010) is used to calculate polarimetric variables from the WRF outputs with different MP schemes. The polarimetric variables are calculated from only the rain, snow, graupel, and hail categories, when applicable, because of the back scattering from cloud water and cloud ice is minimal. The PRDS uses the T-matrix method (Vivekanandan et al., 1991) to calculate the complex scattering amplitudes from both rain and ice-phase species through numerical integration over the PSDs. Different from the original simulator, the function of raindrop axis ratio and raindrop diameter is fitted from 2DVD observations of seven typhoons (Wen et al., 2018). The function is the same as that described in Chang et al. (2009) as follows:

$$\frac{b}{a} = -1.9223 \times 10^{-4}D^4 + 4.3403 \times 10^{-3}D^3 - 3.3439 \times 10^{-2}D^2 + 4.2514 \times 10^{-2}D + 0.98287. \quad (1)$$

Other configurations are the same as the original version and can be found in Jung et al. (2008, 2010).

2.5. Diagnose of Microphysical Process

In a double moment MP scheme, the hydrometeor mixing ratio (q_x, kg kg^{-1}) and the total number concentration (N_{Tx}, kg^{-1}) are predicted, with the governing equations being

$$\frac{\partial q_x}{\partial t} = -\frac{1}{\rho}\nabla\cdot\left(\rho q_x \overrightarrow{V}\right) + \frac{1}{\rho}\frac{\partial}{\partial z}(\rho q_x V_{Qx}) + \left.\frac{dq_x}{dt}\right|_S + TURB(q_x), \quad (2)$$

$$\frac{\partial N_{Tx}}{\partial t} = -\nabla\cdot\left(N_{Tx}\overrightarrow{V}\right) + \frac{\partial}{\partial z}(N_{Tx}V_{Nx}) + \left.\frac{dN_{Tx}}{dt}\right|_S + TURB(N_{Tx}), \quad (3)$$

where $\overrightarrow{V}$ is the air velocity vector, and V_{Qx} is the mass-weighted terminal fall speed. Subscript x refers to any hydrometeor species. Terms on the right hand of equations (2) and (3) indicate advection/divergence, sedimentation, source/sink of different microphysical processes, and turbulent mixing, respectively. The source/sink terms, $\left.\frac{dq_x}{dt}\right|_S$ and $\left.\frac{dN_{Tx}}{dt}\right|_S$, are determined by the transfer rates of microphysical processes such as nucleation, condensation/evaporation, deposition/sublimation, freezing/melting, collisions, etc.

To understand the performances of different MP schemes, the RSD parameters and rates of microphysical processes are diagnosed. The RSD parameters, mass-weighted mean diameter D_{mr} (mm) and generalized intercept parameter N_{wr} (mm^{-1} m^{-3}), can be calculated from the predicted rain mixing ratio q_r and total number concentration N_{Tr} via

Table 1
Summary of Experiments of Different Microphysical Parameterization Schemes

Experiments	Prognostic number concentrations	Descriptions
Morr	Rain, ice, snow, graupel	Morrison double-moment scheme (Morrison et al., 2005), with default prescribed number of cloud droplets of 2.5×10^{8} m^{-3}
ThomA	Cloud, ice, rain, CCN, IN	Thompson aerosol-aware scheme (Thompson & Eidhammer, 2014)
Thom	Ice, rain	Thompson scheme (Thompson et al., 2008), with default prescribed number of cloud droplets of 10^{8} m^{-3}
WDM6	Cloud, rain, CCN	WRF double-moment 6-class scheme (Lim & Hong, 2010)
Morr_NC1E7	Rain, ice, snow, graupel	Morrison double-moment scheme, with the prescribed number of cloud droplets being set to 10^{7} m^{-3}
Thom_NC1E7	Ice, rain	Thompson scheme, with the prescribed number of cloud droplets being set to 10^{7} m^{-3}

$$D_{mr} = \left[\frac{6\rho q_r}{\pi \rho_w N_{Tr}} \right]^{1/3}, \tag{4}$$

$$N_{wr} = \frac{256}{\pi \rho_w} \frac{\rho q_x}{D_{mr}^4}, \tag{5}$$

where ρ and ρ_w are the densities of air and water, respectively. The production rates of microphysical processes related to the raindrop characteristics are also diagnosed and written out during WRF simulations. The model time step is 15 s and data are output every 10 min. This model output frequency is generally appropriate since this study is only focused on the domain average of the microphysical processes, not the temporal evolution. The microphysical processes affecting q_r and N_{Tr} are summarized in Table 2.

3. RSD Comparison

3.1. Environment

Before comparing the performances of different MP schemes in detail, the simulated environmental conditions are assessed by comparing the simulations with a sounding observation. The observed and simulated skew T-LogP diagrams and vertical wind profiles at the Jiangning rawinsonde site (square in Figure 1) at 0600 UTC 24 July 2014 are shown in Figure 2. The observed sounding shows a very moist environment with relative humidity over 80% below 400 hPa. A low lifting condensation level of ~73 m and a freezing level at ~550 hPa indicate a deep layer of warm clouds. A moderate convective available potential energy of ~1,404 J kg^{-1} is rather uniformly distributed between 900 and 150 hPa.

All simulations show nearly saturated environments below 400 hPa, which is more humid than the observation. The lifting condensation levels from all simulations are slightly lower than the observed, and the simulated freezing levels have good agreement with the observation, suggesting that the deep layer of warm clouds is simulated well. The simulated convective available potential energy values and vertical distributions from all experiments are similar to the observation, except for the WDM6 experiment, which is attributed to its relatively low surface temperature. Generally, the simulations using different MPs produce environmental conditions close to observed, which allow for reasonable simulations of RSD.

3.2. Simulated Rainband

During the analysis period, Matmo was rated as a tropical storm with a minimum sea level pressure of 992 hPa and a maximum surface wind of 20 m s^{-1}. All simulations reproduced the track and intensity of typhoon Matmo reasonably well (not shown) and capture the asymmetric structure of precipitation, with the major precipitation area located on the northwest side of the typhoon (Figure 3). Also, all experiments simulated three apparent rainbands at correct locations, although the shape and detailed structure may not be sufficiently close to the observation. Due to the limited coverage of LSRD, this study only focuses on the inner rainband (rainband I in Figure 3a).

A snapshot of the observed and simulated Z_H and Z_{DR} of the inner rainband at 1100 UTC on 24 July is shown in Figure 4. Compared to the observation (Figure 4a), simulated rainbands have similar banded structures, although less organized. All simulations have a similar range of Z_H values (Figures 4b–4f), which are close to the observation. In contrast to Z_H, the simulations produce quite different Z_{DR} values among different MP

Table 2
List of the Microphysical Processes Related to Rain Species; QR and NR Indicate Change in Mixing Ratio and Number Concentration, Respectively

Process of QR	Processes of NR	Description
QRAU	NRAU	Autoconversion of cloud droplets to form rain
QRACI	NRACI	Accretion of rain by all ice species, including ice, snow, graupel, and hail, if applicable. It is worth noting that Thompson schemes process this procedure for the whole model column at the same time. Below the freezing level, the collection of raindrops by ice particles may enhance the melting process, which would produce positive values of QRACI and NRACI
QRFZ	NRFZ	Freezing of rain
QREVP	NREVP	Evaporation of rain. In WDM6 scheme, evaporation and condensation rates of rain are calculated at the same time. Negative values indicate evaporation, while positive values indicate condensation
QRSML	NRSML	Melting of snow to form rain
QRGML	NRGML	Melting of graupel to form rain
QRAC	-	Accretion of cloud droplets by rain
-	NRC	Self-collection of rain

schemes. Experiment Morr generally overestimates the Z_{DR} values compared to the observations (Figures 4h and 4i). Considering both Z_H and Z_{DR}, results would suggest that simulation Morr has a lower raindrop number concentration and a larger mean raindrop size than the observation. ThomA, Thom, and WDM6 experiments produce Z_{DR} values that are generally comparable to the observations for Z_H over 35 dBZ, while Z_{DR} values are generally underestimated for Z_H less than 35 dBZ.

3.3. DSD Comparisons

To further evaluate the simulations quantitatively, the joint frequency distribution normalized by the maximum frequency of Z_H and Z_{DR} is produced for both observation and simulations and shown in Figure 5. The observed and simulated Z_H and Z_{DR} at the lowest elevation angle of 0.5° within the 150 km maximum observation radius of LSRD during 0800 and 1600 UTC are presented. The peak frequencies of Z_H and Z_{DR} are at ~23 dBZ and ~0.25 dB, respectively (Figure 5a). The modal distribution (frequency > 50%) extends from 15 to 35 dBZ in Z_H and from −0.1 to 0.75 dB, and less than 2.5% of the peak frequency exceeds 50 dBZ in Z_H and 1.9 dB in Z_{DR}.

The Morr simulation has modal distributions that extend from 0 to 40 dBZ for Z_H and from 0 to 1.8 dB for Z_{DR} (Figure 5b), which are much wider than the observations. As Z_H increases, Z_{DR} increases much faster in Morr simulation than in observations (Figure 5b), suggesting that the Morr simulation produces precipitation with larger raindrop sizes and a lower total number concentration than the observation, especially for Z_H over 35 dBZ. ThomA, Thom, and WDM6 simulations have similar frequency distributions with the narrowest distribution of 5% frequencies (Figures 5c–5e). Their Z_{DR} values are generally below 1 dB, which is in a good agreement with observations. Among the simulations, ThomA shows the greatest fidelity to the radar observations in terms of the frequency distribution for Z_H between 20 and 40 dBZ. ThomA has a relatively lower increase rate of Z_{DR} as Z_H increases, and a wider distribution of Z_{DR} for a given Z_H than the other simulations, again indicating a good agreement with the radar observations. The relative performances of each MP scheme are quite similar to those found in Brown et al. (2016).

To further evaluate the simulated RSDs, a joint frequency distribution of D_{mr} and N_{wr} is calculated and normalized by the maximum occurrence frequency for observation and simulations during 0800 and 1600 UTC. The rainfall rate of 10 mm hr^{-1} is used to separate stratiform (less than 10 mm hr^{-1}) and convective (greater than 10 mm hr^{-1}) precipitation (Chang et al., 2009; Wang, Zhao, et al., 2016). The observations from both 2DVD and LSRD clearly show that the number concentration (raindrop size) is slightly higher (lower) than those of typical maritime type convective precipitation (Bringi et al., 2003) (Figure 6a).

Consistent with the higher increase rate of Z_{DR} as Z_H increases, the D_{mr}-N_{wr} distribution of Morr experiment generally shows greater D_{mr} and lower N_{wr} than the observations (Figure 6b). The D_{mr}-N_{wr} characteristics of
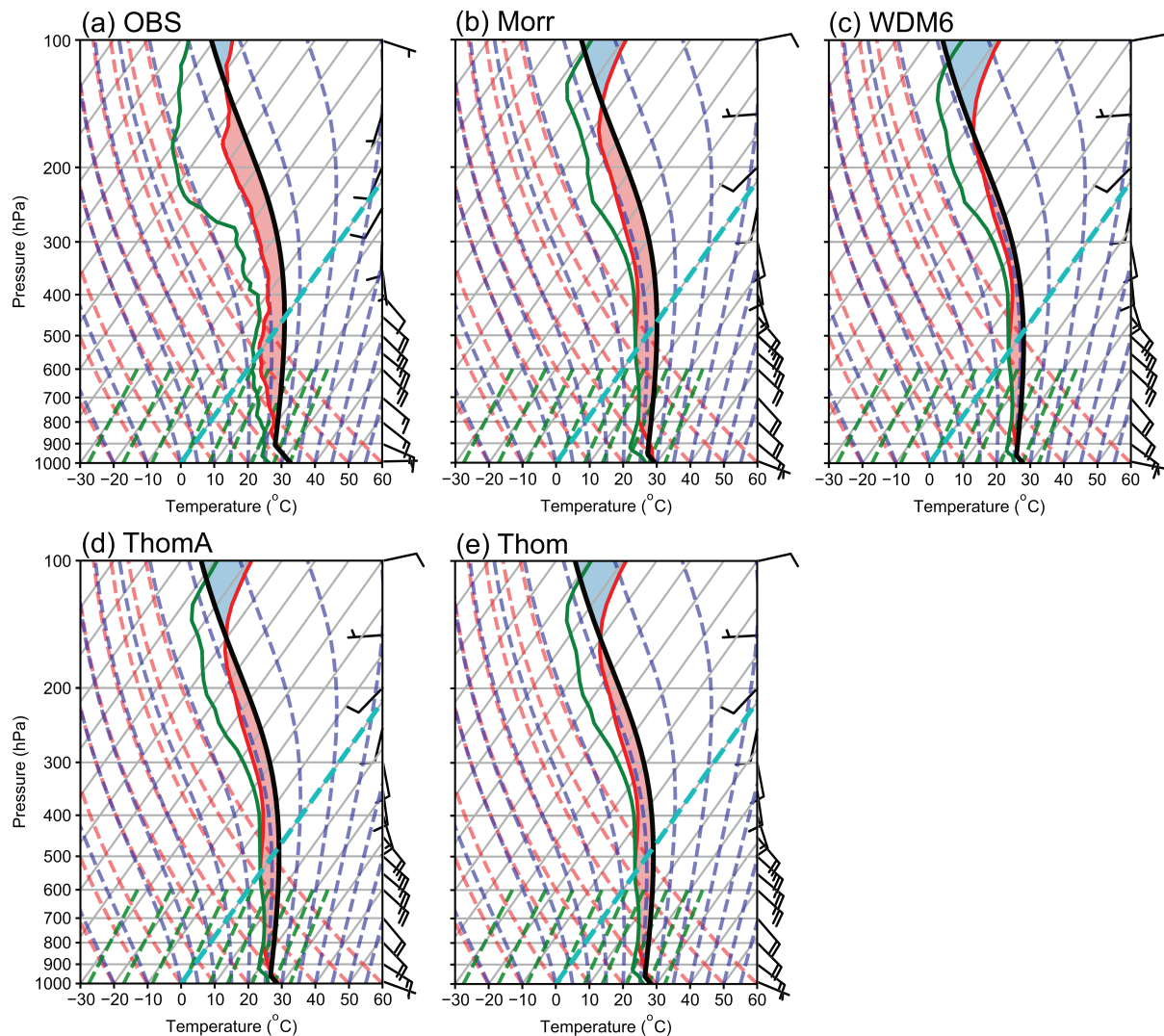
Figure 2. The (a) observed and (b–e) simulated skew T-LogP diagram and vertical wind profile at the Jiangning rawinsonde station (square in Figure 1) at 0600 UTC 24 July 2014. The red and green lines are temperature and dewpoint temperature profiles, respectively. The black curve is the ascending path of a surface-based parcel. Panel (b) is the simulation from Morrison scheme, (c) from WDM 6-class scheme, (d) from the Thompson aerosol-aware scheme, and (e) from the Thompson scheme.

the simulated convection in experiment Morr are close to those of continental convection, in terms of the means and distributions of D_{mr}-N_{wr} (up-right portion of Figure 7b). The WDM6 simulation clearly produces higher N_{wr} and lower D_{mr} than the observation for stratiform precipitation (Figure 7c). The microphysical characteristics of WDM6 simulation is close to those of maritime type, while still overestimating (underestimating) the mean drop size (total number concentration). ThomA simulation produces a similar vertical pattern of D_{mr}-N_{wr} distribution to the observations (Figure 6d), suggesting that the microphysical transition from stratiform precipitation to convective precipitation is mostly attributed to the increase of raindrop number concentration. ThomA simulation also shows the greatest fidelity to the observation according to the generally distribution of D_{mr} and N_{wr}, although the raindrop sizes are somewhat underestimated. The convective precipitation of ThomA simulation also has higher number concentration and smaller mean diameter than the maritime type convective precipitation. The Thom simulation has similar characteristics of stratiform precipitation as the ThomA simulation, while overestimating (underestimating) the drop size (number concentration) of the convective precipitation (Figure 6e). Overall, experiment ThomA produces the best simulation of the RSD based on both Z_H-Z_{DR} and D_{mr}-N_{wr} frequency distributions.
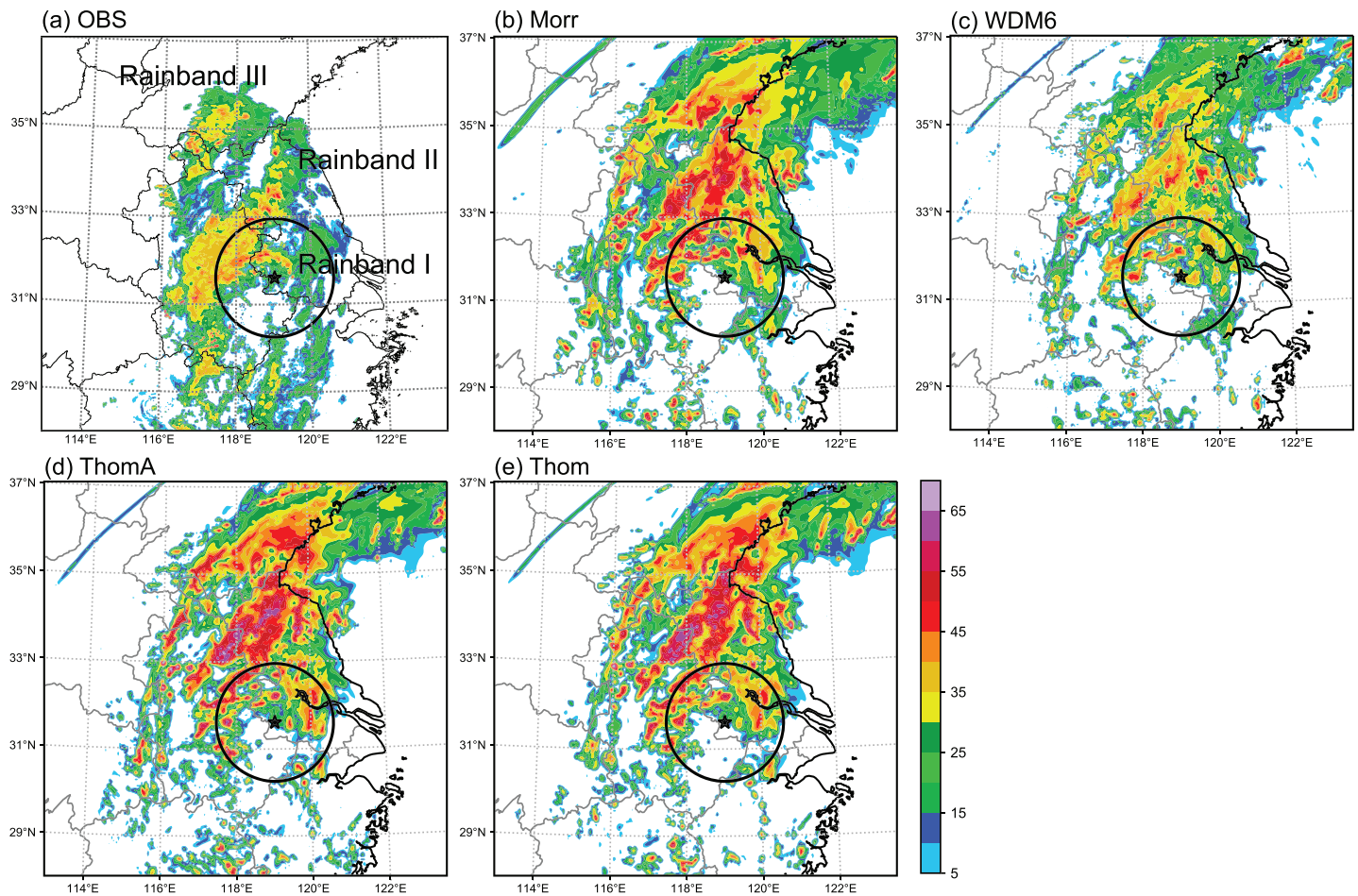
Figure 3. The composite reflectivity (dBZ) from (a) the observation and the simulations using microphysics schemes of (b) Morrison scheme, (c) WDM 6-class scheme, (d) Thompson-aerosol aware scheme, and (e) Thompson scheme at 1100 UTC 24 July 2014. The stars indicate the location of LSRD, and the circles are the maximum observation range of LSRD.

4. Microphysical Processes

The prior analyses show that simulations with different microphysics schemes produce variable DSD characteristics, especially for convective precipitation. In this section, the dominant microphysical processes that produce the different DSD characteristics are further diagnosed for convective precipitation from all simulations. The convective regions are first classified using a classic algorithm proposed by Steiner et al. (1995). This method can well separate the convective regions from all simulations (figure not shown). Each of the transfer rates related to rainwater mass content (Q_r) and raindrop total number concentration (N_{Tr}) are integrated over each model column and then averaged over the convective regions to identify the dominant process. Moreover, the mean vertical profiles of the transfer rates within the convective regions are analyzed to examine the heights that each of microphysical processes is most active.

4.1. Dominant Rainwater-Related Microphysical Processes

The domain integrated transfer rates related to rain production are calculated and plotted in Figure 7. In general, the dominant rainwater source is the accretion of cloud droplets by raindrops in all experiments (Figure 7a), indicating a warm-rain-dominant rainwater growth, consistent with earlier observational analyses on this case (Wang, Zhao, et al., 2016). The dominant rainwater sink is the riming of raindrops onto ice particles in Thom and WDM6 experiments, while the major sink in Morr and ThomA experiments is rainwater evaporation (Figure 7a). Among all experiments, ThomA produces the greatest accretion rate of over 0.1 g s^{-1}. The secondary rainwater source is melting of snow or graupel particles, but it is generally
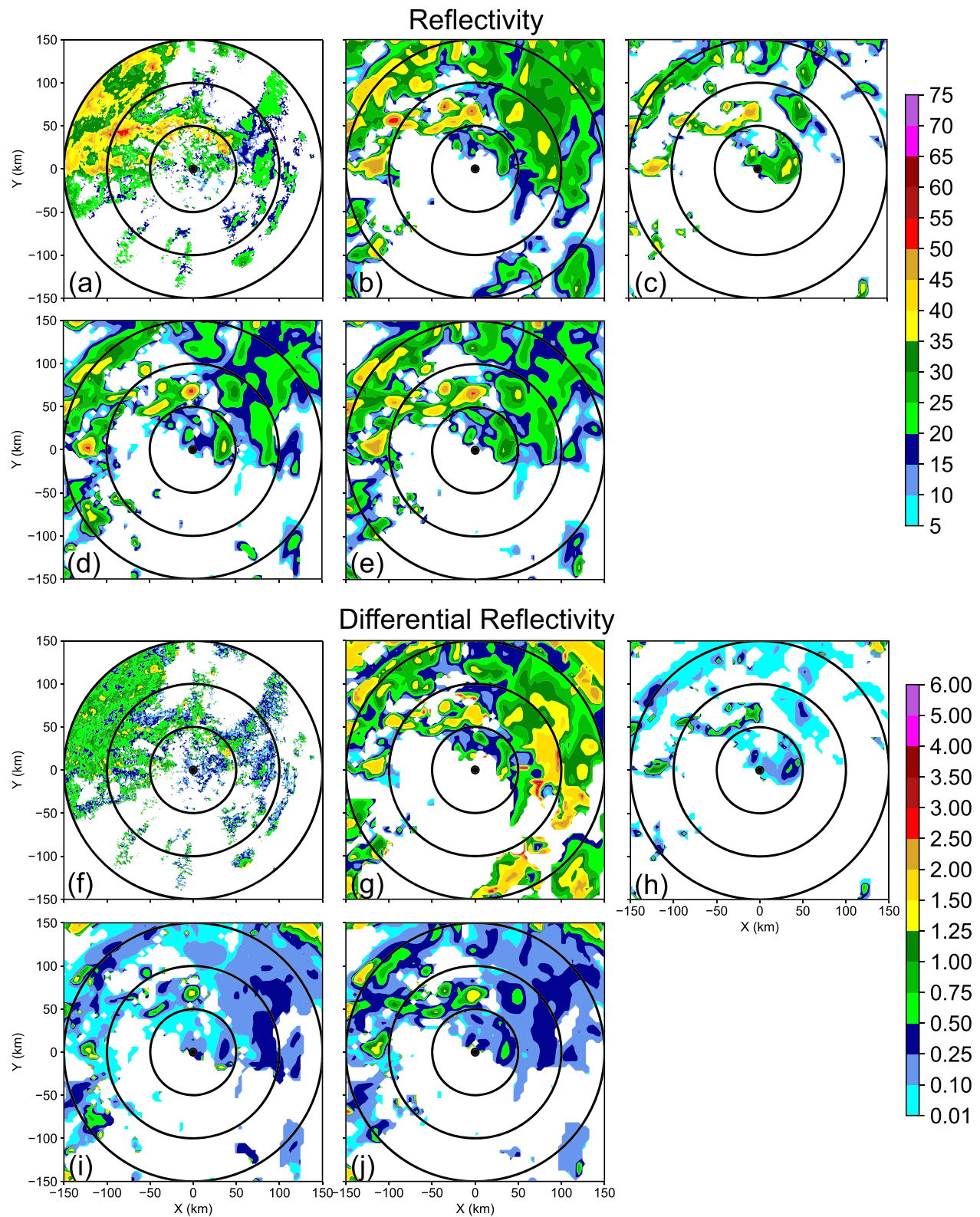
Figure 4. The (a–e) reflectivity and (f–j) differential reflectivity at 0.5° elevation from the (a, f) LSRD radar and simulations using (b, g) the Morrison scheme, (c, h) the WDM 6-class scheme, (d, i) the Thompson aerosol-aware scheme, and (e, j) the Thompson scheme at 1100 UTC 24 July 2014. The black circles are range rings of 50, 100, 150 km, respectively.
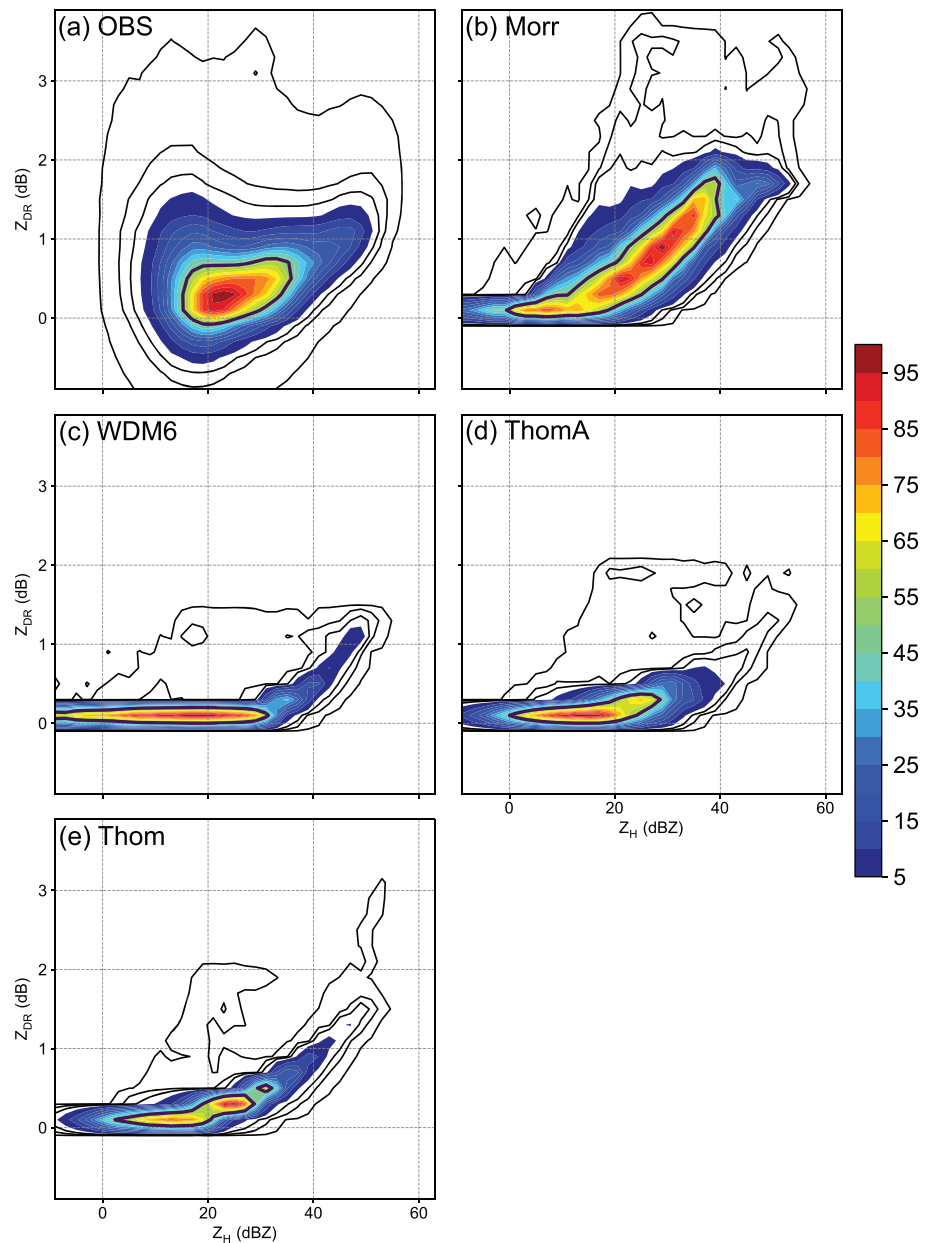
Figure 5. Frequency of occurrences (color shaded) of Z_H (dBZ) and Z_{DR} (dB) normalized by the maximum frequency of (a) the retrieved DSDs from LSRD at a 0.5° tilt, and simulated DSDs at the same tilt from (b) Morr, (c) WDM6, (d) ThomA, and (e) Thom experiments. Thin black contours are percentages at 0.1%, 1%, and 2.5%, and thick black contour is at 50%.

one order of magnitude smaller than the accretion rate except for the WDM6 simulation. In experiment WDM6, the production rate of Q_r from melting is comparable to the accretion process, which may be attributed to the very high riming rate that produces a large amount of graupel particles in the scheme. Experiments ThomA and WDM6 also produce some of the rainwater via autoconversion.

The primary source of N_{Tr} is the autoconversion process, while the primary sink of N_{Tr} is the coalescence between raindrops (Figure 7b). The autoconversion rates from ThomA and WDM6 experiments are an order of magnitude greater than those of other experiments, and similar to the coalescence rates. The contributions from melting processes to N_{Tr} are almost negligible except for experiment WDM6. Consistent with the Q_r source of experiment WDM6, the melted ice particles still have certain contribution to N_{Tr}, due to
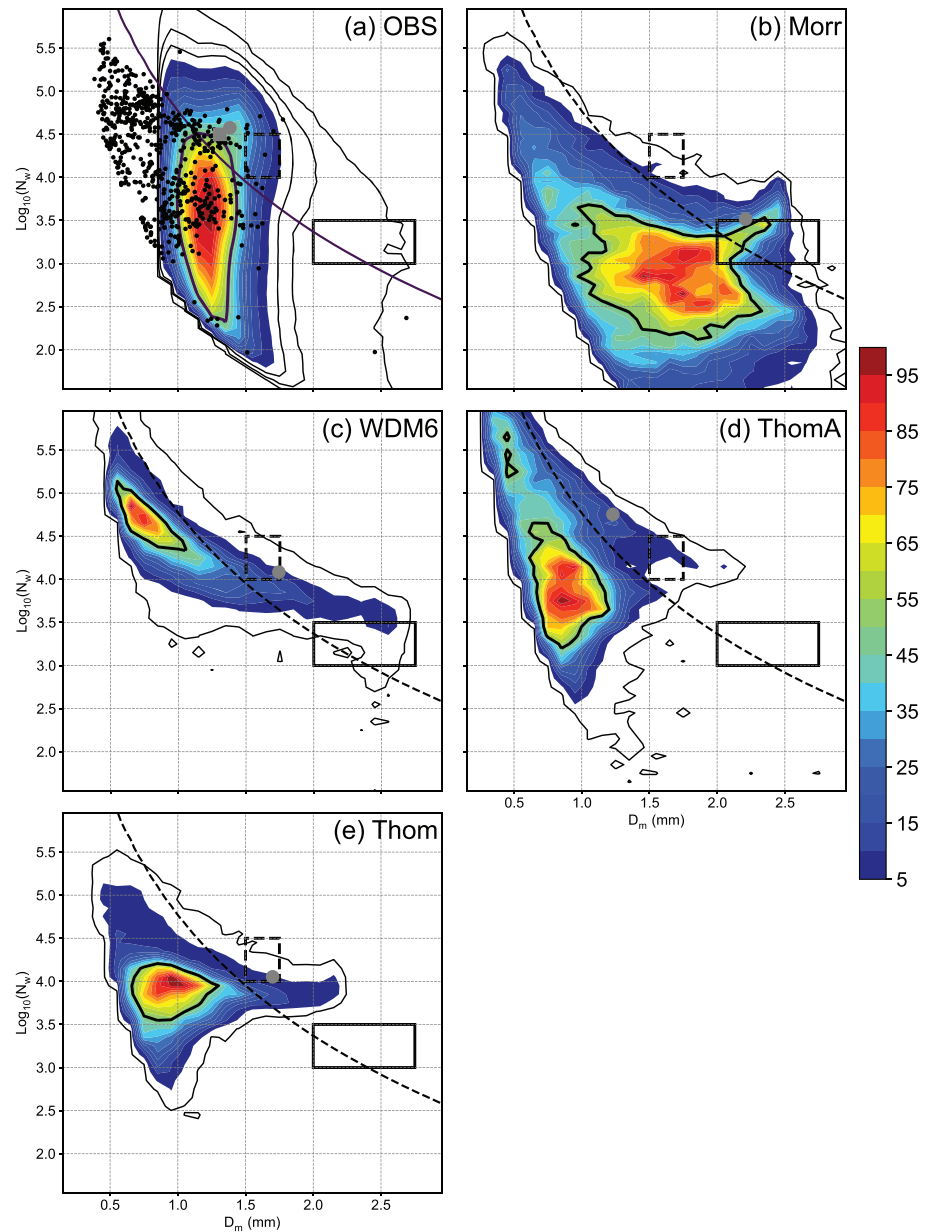
Figure 6. Frequency of occurrences (color shaded) of D_{mr} (mm) and logarithmic N_{wr} (mm^{-1} m^{-3}) of (a) the retrieved DSDs from LSRD at a 0.5° tilt, and simulated DSDs at the same tile from (b) Morr, (c) WDM6, (d) ThomA, and (e) Thom experiments. The black dots in (a) indicate the D_{mr} and N_{wr} values calculated from 2DVD. The dashed curve represents the rainfall rate of 10 mm hr^{-1}. The two rectangles represent the maritime (dashed) and continental (solid) types of convective precipitation, respectively. The gray dots in each frame indicate the mean value of D_{mr} and N_{wr} from LSRD and simulations for rainfall rate over 10 mm hr^{-1}. The gray square in (a) is the mean value from 2DVD observation.

a large number of raindrops collected by ice particles. The coalescence rate of raindrops is commonly proportional to $-N_{Tr}$ in microphysics schemes (Beheng, 1994). The coalescence process should largely depend on the number of raindrops produced by the autoconversion process, which leads to the depletion rates by the coalescence process quite close to the autoconversion rate in all experiments.

Overall, the convective precipitation from all experiments are generally warm-rain-dominant according to both Q_r and N_{Tr} productions, consistent with observational analyses (Wang, Zhao, et al., 2016). However, experiment WDM6 still has considerable contributions from ice processes. The accretion process and auto-conversion process are the major source of rainwater content and raindrop number concentration,
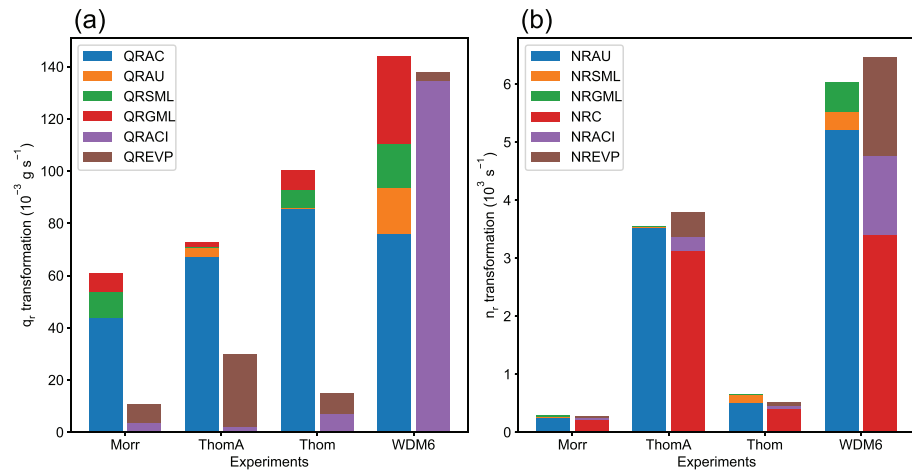
Figure 7. The transfer rates of the source (left column) and sink (right column) terms for (a) rainwater mixing ratio and (b) raindrop number concentration from each experiment. In the acronyms, QR and NR indicate change in mixing ratio and number concentration, respectively. "AC" represents accretion, "AU" represents autoconversion, "SML" represents snow melting, "GML" represents graupel melting, "ACI" represents accretion of rain by all ice species, "EVP" represents evaporation, "C" represents self-collection of raindrops. Descriptions of the acronyms can be further referred to Table 2.

respectively. The primary sink of Q_r is the collection of raindrops by ice particles through riming, and the primary sink of N_{Tr} is the coalescence of raindrops. Although the convective RSD characteristics of experiment Morr appear to be of continental convection type, the rainwater mainly comes from the warm-rain processes. In contrast, in WMD6, the convective RSD characteristics is close to the maritime type while the ice particle melting substantially contributes to the rainwater production. In general, ThomA and Thom schemes produce warm-rain-dominant rainwater production and RSD characteristics that are more of the maritime type, which is more consistent with the observations.

4.2. Vertical Evolution of Microphysical Processes

The vertical profiles of mean mass contents and number concentrations of cloud, rain, snow, and graupel within the convective regions are plotted in Figure 8 along with the mass-weighted mean diameter. All experiments had comparable cloud water content (Q_c) from the ground to the 10 km height with the maxima at around the freezing level of 5.2 km, and experiment Thom produces the greatest Q_c among all experiments (Figure 8a). The simulated number concentrations of cloud droplets (N_{Tc}) from ThomA and WDM6 schemes are an order of magnitude lower than the fixed N_{Tc} of Thom and Morr schemes. The values of Q_c and N_{Tc} imply that the cloud droplets of ThomA and WDM6 should be much larger in size than those of Thom and Morr. The rainwater mass content from different experiments has similar vertical variations that increase from 10 km down to the maximum at 4 km and then decrease toward the ground (Figure 8b). Experiments ThomA and Morr have the highest and the lowest rainwater content, respectively. The simulated N_{Tr} has similar vertical distributions as Q_r, while their maxima are at about 5 km. The combination of Q_r and N_{Tr} makes D_{mr} increase toward the ground (Figure 8g). Experiment ThomA exhibits the lowest rainwater D_{mr} increase rate among all experiments, corresponding to the smallest D_{mr} in Figure 6. The water contents of snow and graupel show substantial differences, suggesting quite different ice processes with different microphysics schemes (Barnes & Houze, 2016). WDM6 has the lowest snow content (Q_s) and the highest graupel content (Q_g), which might be due to active transfer of snow into graupel through the riming process (Figure 7a).

The vertical variations of microphysical processes related to Q_r and N_{Tr} are then examined. Figures 9 and 10 show the vertical profiles averaged over convective regions of the transfer rates related to Q_r and N_{Tr}, respectively. The rainwater conversion from cloud water through accretion becomes dominant below the freezing level (Figure 9a), with the maximum transfer rate at around 4.5 km corresponding to the level of maximum cloud water content (Figure 8a). Experiment ThomA has the highest rate and experiment Morr has the lowest rate, consistent with the corresponding Q_r profiles (Figure 8b). The autoconversion process is active from
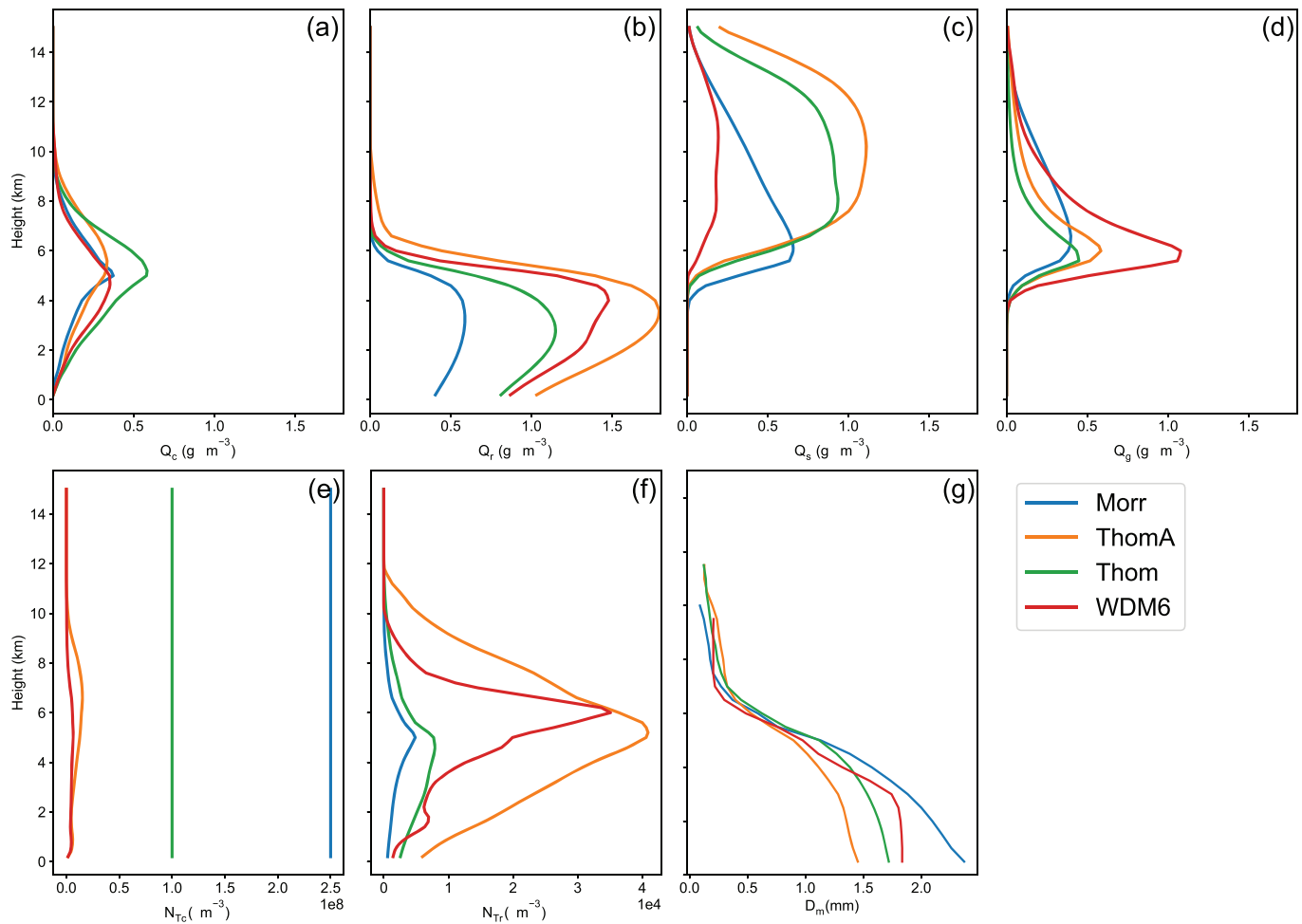
Figure 8. Vertical profiles of the mass contents of (a) cloud water, (b) rain water, (c) snow, and (d) graupel, the total number concentrations of (e) cloud droplets and (f) raindrops, and (g) mass-weighted mean diameter of raindrops, averaged over the convective regions.

the ground to about 10 km in all simulations, with the rates from Morr and Thom experiments being much smaller than those of other two experiments in terms of both water content (Figure 9b) and number concentration (Figure 10a). Experiment WDM6 has significantly higher rainwater autoconversion rates for mass production than ThomA while the number production rates are comparable, suggesting that the raindrop sizes in WDM6 simulation should be larger than those of ThomA simulation.

Rainwater evaporation is mostly active below 2 km (Figures 9c and 10c), consistent with the evaporation signature below 2 km identified from polarimetric measurements (Wang et al., 2018). ThomA experiment has the highest rainwater evaporation rate below 2 km, which is most likely related to the large concentration of small raindrops that evaporate much faster than larger raindrops. A large number of raindrops from WDM6 experiment are, however, evaporated between 2 and 8 km (Figure 10c), which is almost half of the corresponding N_{Tr} production through autoconversion (Figure 10a). The melting processes are mostly active within a shallow layer below the freezing level. WDM6 experiment produces a larger amount of rainwater and raindrops through the melting of graupel, matching to the much higher riming rates immediately above the freezing level (Figures 9f and 10f). The reduction in number concentration and the increase in mean diameter (Figure 8) are mainly attributed to the coalescence process (Figure 10b). ThomA and WDM6 experiments have much higher coalescence rates than Morr and Thom experiments from the surface up to 7 km.

Base on the vertical variations of the microphysical process rates, the increases of D_{mr} below 4 km in different simulations can be primarily attributed to the coalescence and evaporation processes, especially the former. The coalescence rate is tightly related to the rainwater content and number concentration produced by the
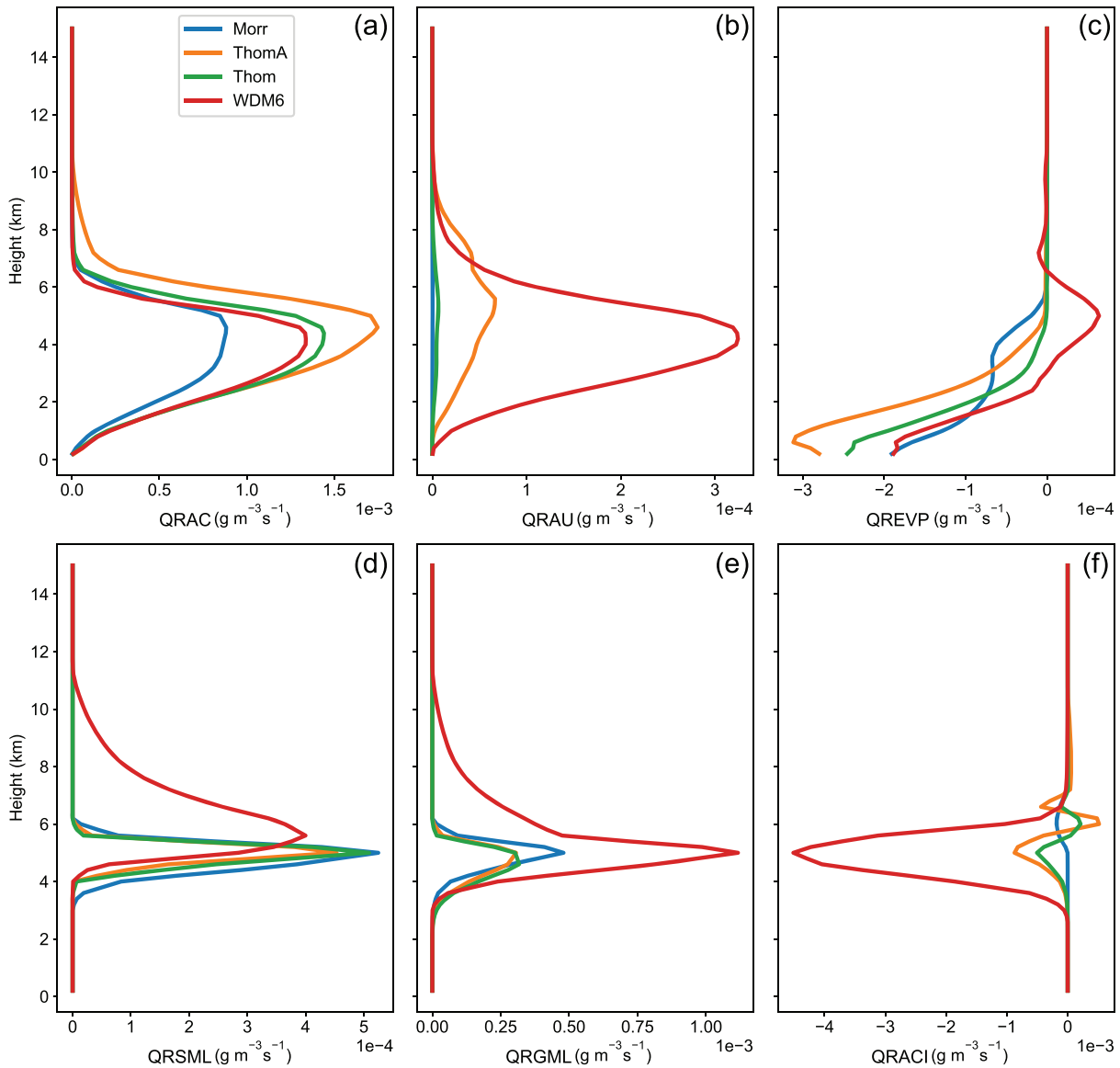
Figure 9. Vertical profiles of the mass content transfer rates of (a) accretion, (b) autoconversion, (c) evaporation, and (d) snow melting, (e) graupel melting, and (f) riming processes averaged over the convective regions.

autoconversion process. The precipitation DSD of ThomA has not reached its equilibrium state even near the surface (Figure 10b), which can be an important reason for the extremely high number concentration and small raindrops.

In the two-moment bulk MP schemes examined, the raindrop total number concentration is directly predicted, while the mass-weighted mean diameter of raindrops is diagnosed from Q_r and N_{Tr}. Therefore, N_{Tr} prediction also strongly impacts the simulated raindrop sizes. All experiments have their own N_{Tr} maxima and similar D_{mr} near the freezing level (Figure 8) owing to the activation of the autoconversion process, and N_{Tr} (D_{mr}) decreases (increases) toward the ground through the coalescence and evaporation of raindrops (Figures 9 and 10). Among all experiments, ThomA produces the highest N_{Tr} near the freezing level, corresponding to the highest N_{Tr} and smallest D_{mr} near the surface. As N_{Tr} near the freezing level decreases, N_{Tr} (D_{mr}) generally decreases (increases) in Thom and Morr simulations. Although WDM6 experiment also has a high N_{Tr} near the freezing level through autoconversion, very active evaporation below 6 km height substantially reduces N_{Tr} and increases D_{mr} toward the ground. Overall, the number concentration of raindrops
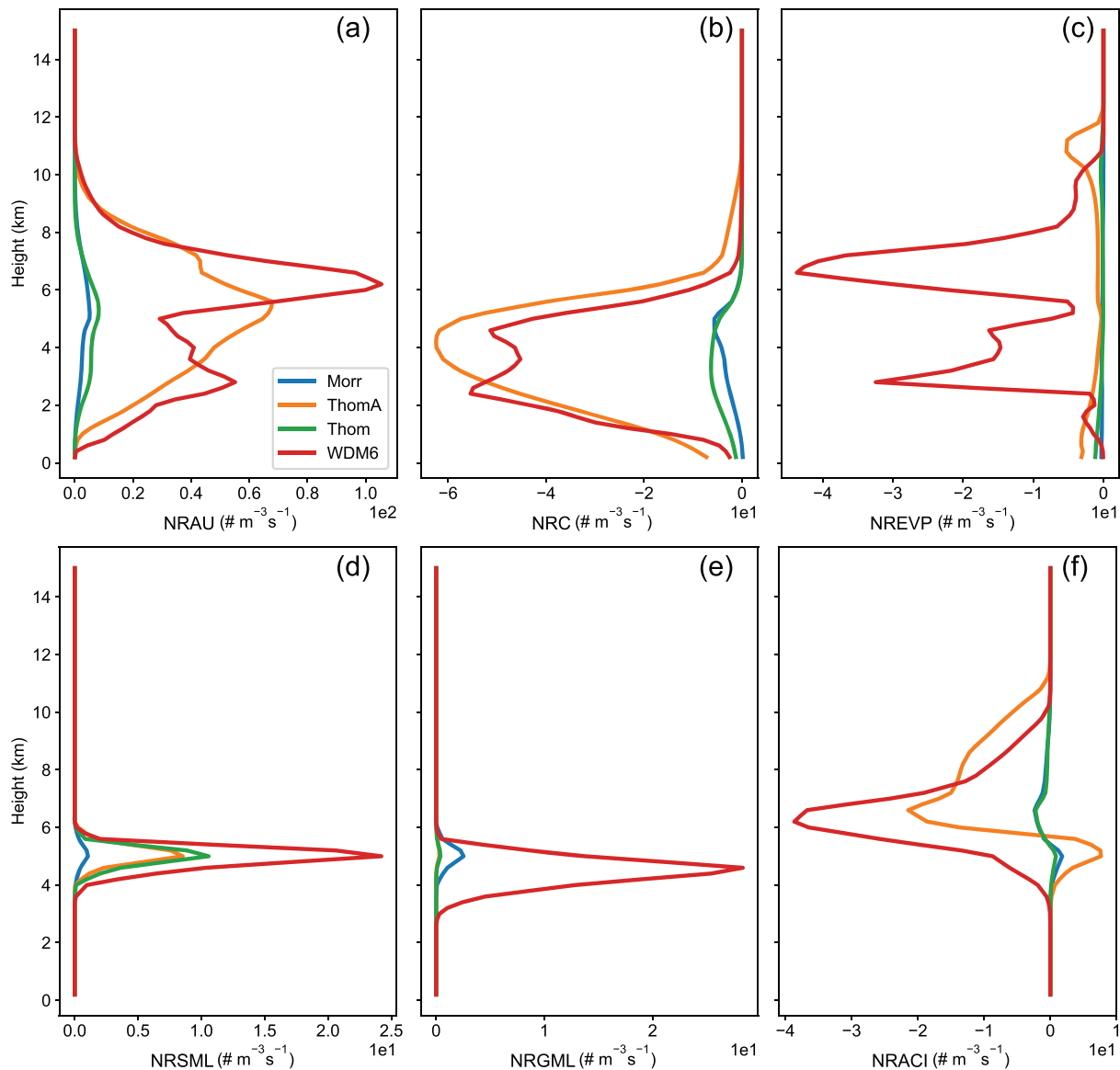
Figure 10. Vertical profiles of the total number concentration transfer rates of (a) autoconversion, (b) coalescence, (c) evaporation, and (d) snow melting, (e) graupel melting, and (f) riming processes averaged over the convective regions.

near the freezing level produced by the autoconversion process apparently affects the vertical evolution of RSDs, and naturally the near surface RSD, suggesting that the autoconversion process plays a dominant role on the RSD characteristics.

5. Sensitivity Tests

The transfer rate of cloud water into rain water through the autoconversion process is tightly connected to the cloud droplet size distribution (Pruppacher & Klett, 2010). ThomA and Thom schemes generally have the same physical framework to describe the microphysical processes. The major difference is that ThomA predicts N_{Tc} using the climatological CCN profiles, while Thom scheme uses a preset N_{Tc} value. The N_{Tc} predicted by ThomA scheme is one magnitude lower than the preset N_{Tc} of Thom scheme, which may directly lead to different autoconversion rates in the experiments, and thus quite different RSD characteristics. Since ThomA experiment has the best agreement with the observations in terms of both RSD characteristics and microphysical processes, therefore the N_{Tc} predicted by ThomA is considered more accurate.
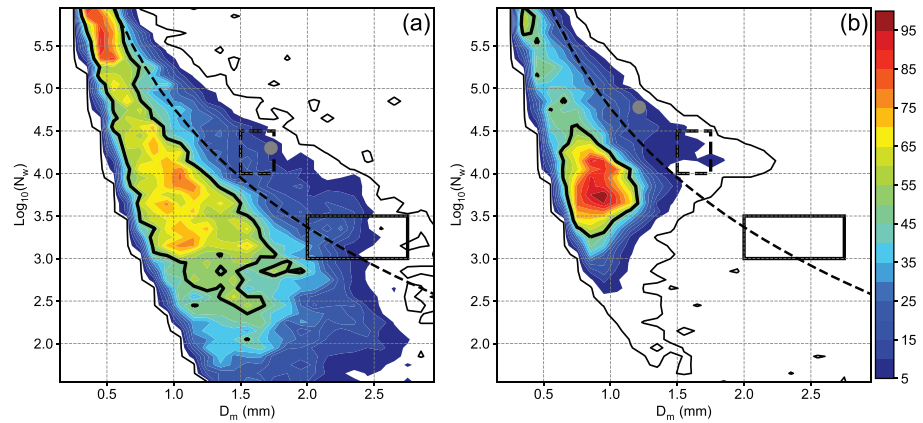
Figure 11. Similar to Figure 6, except (a) from Morr_NC1E7 and (b) from Thom_NC1E7.

To verify the impact of N_{Tc} on the RSD forecasts, two sensitivity experiments are conducted by setting the N_{Tc} values of Morr and Thom schemes to 10^7 m^{-3}, which is close to the predicted N_{Tc} from ThomA experiment. After N_{Tc} is reduced, the predicted D_{mr}-N_{wr} distribution is substantially modified and becomes much closer to the observations (Figure 11). The D_{mr}-N_{wr} distributions from Thom_NC1E7 and Morr_NC1E7 are shifted toward upper left corner, indicating the number concentration and mean size are increased and reduced, respectively. The RSDs from these two experiments over the convective regions generally exhibit the same features as ThomA experiment, suggesting that the number concentration of cloud droplets plays a predominant role on the RSD prediction.

To examine the responses of microphysical processes to the N_{Tc} change, the domain integrated transfer rates related to rain production from the two sensitivity experiments are calculated and plotted in Figure 12. After
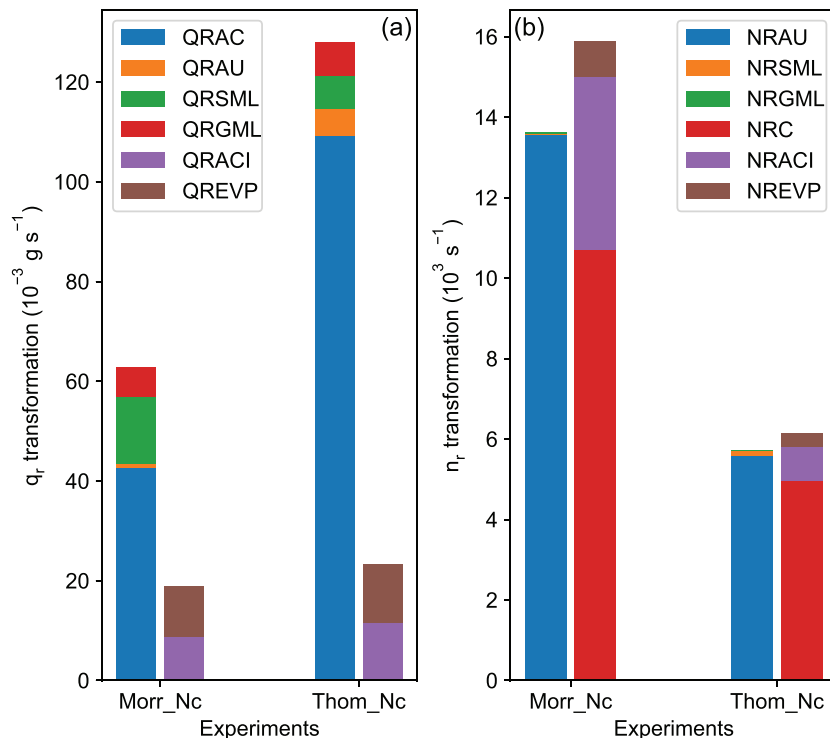

Figure 12. The transfer rate of the source (left column) and sink (right column) terms for (a) rainwater mixing ratio and (b) raindrop number concentration from two sensitivity experiment.

the N_{Tc} is reduced, the rain water production is still warm-rain dominant (Figure 12a), but the Q_r and N_{Tr} transfer rates are significantly modified. The autoconversion rates are significantly enhanced for both Morr_NC1E7 and Thom_NC1E7 experiments (Figure 12). The N_{Tr} produced by autoconversion process in Morr_NC1E7 (Thom_NC1E7) experiment (Figure 12b) is almost 50 (10) times that of Morr (Thom) experiment (Figure 7b). Consequently, the coalescence process and the riming process are also substantially enhanced. The accretion rate from Morr_NC1E7 is almost the same as that from Morr. The melting of snow and graupel has increased, consistent with the increasing raindrops collected by ice particles. The Q_r growth rates produced by the accretion and autoconversion processes from Thom_NC1E7 are greatly increased to a magnitude somewhat larger than that of ThomA.

By reducing N_{Tc} of Thom and Morr schemes to a value similar to those simulated by ThomA scheme, the simulations of Thom_NC1E7 and Morr_NC1E7 become much closer to the observations, according to the RSD characteristics and raindrop-related transfer rates (Figures 7 and 12). In general, sensitivity experiments indicate that N_{Tc} is a key factor affecting the RSD prediction within bulk MP schemes for Typhoon Matmo.

6. Conclusions and Discussions

In this study, Typhoon Matmo that made landfall over eastern China are simulated using four different bulk MP schemes within the WRF model and verified against observations collected by a polarimetric radar and a 2DVD. The simulated RSDs are validated using a PRDS to see if the MP schemes can reproduce the unique RSD characteristics of the inner rainband in Typhoon Matmo, whose convective precipitation is generally consisted of raindrops that are of smaller sizes and higher number concentrations than typical maritime type convection. To further investigate the dominant microphysical processes controlling the RSD characteristics, the simulated microphysical processes are examined through raindrop mass content and number concentration source/sink diagnoses. Moreover, sensitivity experiments are conducted to identify the key factor responsible for the unique RSD characteristics of Typhoon Matmo.

The joint frequency distributions of Z_H-Z_{DR} and D_{mr}-N_{wr} are produced for both the observations and simulations to evaluate the RSD simulations quantitatively. The Morrison simulation produced precipitation with larger raindrops and lower number concentrations than the observation, generally exhibiting continental type convective precipitation. The microphysical characteristics of both Thompson and WDM6 simulations are close to the maritime type convection, while still overestimating (underestimating) the raindrop size (number concentration) compared to the observations. The simulation using the aerosol-aware Thompson scheme shows the greatest fidelity to the observations according to the distributions of Z_H-Z_{DR} and D_{mr}-N_{wr}, while the raindrop sizes are somewhat underestimated. Among the four MP schemes examined, only the aerosol-aware Thompson scheme is able to reproduce the unique observed RSD characteristics of the inner rainband in Typhoon Matmo.

The convective precipitation from all experiments are generally warm-rain-dominant according to both rain-water content and raindrop number concentration production, consistent with observations. The accretion and autoconversion processes are the major sources of rainwater content and raindrop number concentration, respectively. Although the convective RSD characteristics of Morr experiment appear of the continental type convection, the rainwater mainly comes from the warm-rain processes. In contrast, the convective RSD characteristics of WDM6 is close to the maritime type, while the melted ice particles substantially contribute to the rainwater production. In general, ThomA and Thom schemes produced rain simulations with the maritime type RSD characteristics and the warm-rain-dominant rainwater production, more or less consistent with observations.

The vertical variations of water contents and number concentrations of cloud, rain, snow, and graupel along with the rain-related microphysical transfer rates are investigated to further identify the dominant microphysical processes influencing the RSD characteristics. From the freezing level downward toward the ground, the predominant microphysical processes are the autoconversion, coalescence, and evaporation processes, respectively. By comparing four simulations using four different MP schemes, the raindrop number concentration near the freezing level, which is dominated by the autoconversion process, plays an important role in affecting the surface RSD characteristics.

Two sensitivity experiments are conducted by reducing the preset cloud droplet number concentration (N_{Tc}) in the Morrison and Thompson schemes to $10^7\,\mathrm{m}^{-3}$, a value close to the value predicted by the ThomA scheme. Results show that the RSD predictions are much improved and have good agreements with the observation by using the reduced N_{Tc}, which was mainly achieved through the invigoration of the autoconversion process. In general, sensitivity experiments indicate that N_{Tc} is a key factor that governs the RSD prediction of Typhoon Matmo within the bulk MP schemes.

Since the RSD characteristics of smaller drops and higher number concentrations than the typical maritime type convection are the common microphysical characteristic of landfalling typhoon precipitation over China, the findings from one representative example of Typhoon Matmo in this study should be able to apply to the landfalling typhoons over East China. Due to warm-rain processes are dominant in all experiments, this study focuses on examining the rainwater-related microphysical processes. However, the ice processes should also affect the RSD characteristics, even though such effects might be minor. For instance, WDM6 is an outlier for riming and melting processes among all experiments, which is most likely related to ice processes. The performances of ice processes in bulk MP schemes require further investigations for landfalling typhoons.

In this study, a N_{Tc} of $10^7\,\mathrm{m}^{-3}$ is found to be the adequate value that produced the RSD close to the observation according to the prediction of Thompson aerosol-aware scheme. This value is a magnitude lower than the typical value of $10^8\,\mathrm{m}^{-3}$ for simulating the maritime precipitation. In situ or remote sensing observation of cloud droplet size distribution would be required to further verify this N_{Tc} value. Since the inner rainband of Typhoon Matmo had a near-saturated environment, N_{Tc} is directly affected by the number of cloud condensation nuclei (CCN). The responses of N_{Tr} to the N_{Tc} reduction is consistent with the responses N_{Tr} to the number of CCN reduction simulated by a spectrum bin scheme in Fan et al. (2017). Thus, the small value of N_{Tc} may imply a low concentration of CCN, which is most likely attributed to the precipitation scavenging by the outer rainband of Typhoon Matmo. However, the bulk schemes may be limited to well represent the interactions between cloud and CCN, due to the prescribed gamma distribution and a relatively simple treatment of cloud nucleation (Khain et al., 2015). In comparison, the spectrum bin scheme would be capable of representing such connections. The impacts of CCN concentration on the cloud concentration and the RSDs of landfalling typhoons are worthy of further investigations. Spectrum bin scheme may be more suitable in the future.

References

Barker, D. M., Huang, W., Guo, Y. R., Bourgeois, A. J., & Xiao, Q. N. (2004). A three-dimensional variational data assimilation system for MM5: Implementation and initial results. *Monthly Weather Review*, *132*(4), 897–914. https://doi.org/10.1175/1520-0493(2004)132<0897:atvdas>2.0.co;2

Barnes, H. C., & Houze, R. A. (2016). Comparison of observed and simulated spatial patterns of ice microphysical processes in tropical oceanic mesoscale convective systems. *Journal of Geophysical Research-Atmospheres*, *121*, 8269–8296. https://doi.org/10.1002/2016JD025074

Beheng, K. D. (1994). A parameterization of warm cloud microphysical conversion processes. *Atmospheric Research*, *33*(1), 193–206. https://doi.org/10.1016/0169-8095(94)90020-5

Black, R. A., & Hallett, J. (2012). Rain rate and water content in Hurricanes compared with summer rain in Miami, Florida. *Journal of Applied Meteorology and Climatology*, *51*(12), 2218–2235. https://doi.org/10.1175/JAMC-D-11-0144.1

Bringi, V. N., & Chandrasekar, V. (2001). *Polarimetric Doppler weather radar: Principles and applications*. Cambridge, U. K.: Cambridge university press.

Bringi, V. N., Chandrasekar, V., Hubbert, J., Gorgucci, E., Randeu, W. L., & Schoenhuber, M. (2003). Raindrop size distribution in different climatic regimes from disdrometer and dual-polarized radar analysis. *Journal of the Atmospheric Sciences*, *60*(2), 354–365. https://doi.org/10.1175/1520-0469(2003)060<0354:RSDIDC>2.0.CO;2

Brown, B. R., Bell, M. M., & Frambach, A. J. (2016). Validation of simulated hurricane drop size distributions using polarimetric radar. *Geophysical Research Letters*, *43*(2), 910–917. https://doi.org/10.1002/2015GL067278

Brown, B. R., Bell, M. M., & Thompson, G. (2017). Improvements to the snow melting process in a partially double moment microphysics parameterization. *Journal of Advances in Modeling Earth Systems*, *9*(2), 1150–1166. https://doi.org/10.1002/2016MS000892

Chang, W.-Y., Wang, T.-C. C., & Lin, P.-L. (2009). Characteristics of the raindrop size distribution and drop shape relation in typhoon systems in the Western Pacific from the 2D video disdrometer and NCU C-band polarimetric radar. *Journal of Atmospheric and Oceanic Technology*, *26*(10), 1973–1993. https://doi.org/10.1175/2009JTECHA1236.1

Dawson, D. T., Mansell, E. R., Jung, Y., Wicker, L. J., Kumjian, M. R., & Xue, M. (2014). Low-level ZDR signatures in supercell forward flanks: The role of size sorting and melting of hail. *Journal of the Atmospheric Sciences*, *71*(1), 276–299. https://doi.org/10.1175/JAS-D-13-0118.1

Didlake, A. C., & Kumjian, M. R. (2018). Examining storm asymmetries in Hurricane Irma (2017) using polarimetric radar observations. *Geophysical Research Letters*, *45*, 13513–13522. https://doi.org/10.1029/2018GL080739

Doviak, R. J., & Zrnić, D. S. (2006). *Doppler radar and weather observations*. 31 East 2nd Street, Mineola, N.Y. 11501: Dover Publications.

Ek, M. B., Mitchell, K. E., Lin, Y., Rogers, E., Grunmann, P., Koren, V., et al. (2003). Implementation of Noah land surface model advances in the National Centers for Environmental Prediction operational mesoscale Eta model. *Journal of Geophysical Research*, *108*(D22), 8851. https://doi.org/10.1029/2002JD003296

Fan, J., Leung, L. R., Rosenfeld, D., & DeMott, P. J. (2017). Effects of cloud condensation nuclei and ice nucleating particles on precipitation processes and supercooled liquid in mixed-phase orographic clouds. *Atmospheric Chemistry and Physics*, *17*(2), 1017–1035. https://doi.org/10.5194/acp-17-1017-2017

Feng, Y.-C., & Bell, M. M. (2019). Microphysical characteristics of an asymmetric eyewall in major Hurricane Harvey (2017). *Geophysical Research Letters*, *46*, 461–471. https://doi.org/10.1029/2018GL080770

Fovell, R. G., Corbosiero, K. L., & Kuo, H.-C. (2009). Cloud microphysics impact on hurricane track as revealed in idealized experiments. *Journal of the Atmospheric Sciences*, *66*(6), 1764–1778. https://doi.org/10.1175/2008JAS2874.1

Hong, S.-Y., Noh, Y., & Dudhia, J. (2006). A new vertical diffusion package with an explicit treatment of entrainment processes. *Monthly Weather Review*, *134*(9), 2318–2341. https://doi.org/10.1175/MWR3199.1

Iacono, M. J., Delamere, J. S., Mlawer, E. J., Shephard, M. W., Clough, S. A., & Collins, W. D. (2008). Radiative forcing by long-lived greenhouse gases: Calculations with the AER radiative transfer models. *Journal of Geophysical Research*, *113*, D13103. https://doi.org/10.1029/2008JD009944

Igel, A. L., Igel, M. R., & van den Heever, S. C. (2014). Make it a double? Sobering results from simulations using single-moment microphysics schemes. *Journal of the Atmospheric Sciences*, *72*(2), 910–925. https://doi.org/10.1175/JAS-D-14-0107.1

Johnson, M., Jung, Y., Dawson, D., Supinie, T., Xue, M., Park, J., & Lee, Y.-H. (2018). Evaluation of unified model microphysics in high-resolution NWP simulations using polarimetric radar observations. *Advances in Atmospheric Sciences*, *35*(7), 771–784. https://doi.org/10.1007/s00376-017-7177-0

Johnson, M., Jung, Y., Dawson, D. T., & Xue, M. (2016). Comparison of simulated polarimetric signatures in idealized supercell storms using two-moment bulk microphysics schemes in WRF. *Monthly Weather Review*, *144*(3), 971–996. https://doi.org/10.1175/MWR-D-15-0233.1

Jung, Y., Xue, M., & Zhang, G. (2010). Simultaneous estimation of microphysical parameters and the atmospheric state using simulated polarimetric radar data and an ensemble Kalman filter in the presence of an observation operator error. *Monthly Weather Review*, *138*(2), 539–562. https://doi.org/10.1175/2009MWR2748.1

Jung, Y., Zhang, G., & Xue, M. (2008). Assimilation of simulated polarimetric radar data for a convective storm using the ensemble Kalman filter. Part I: Observation operators for reflectivity and polarimetric variables. *Monthly Weather Review*, *136*(6), 2228–2245. https://doi.org/10.1175/2007MWR2083.1

Khain, A., Lynn, B., & Shpund, J. (2016). High resolution WRF simulations of Hurricane Irene: Sensitivity to aerosols and choice of microphysical schemes. *Atmospheric Research*, *167*, 129–145. https://doi.org/10.1016/j.atmosres.2015.07.014

Khain, A. P., Beheng, K. D., Heymsfield, A., Korolev, A., Krichak, S. O., Levin, Z., et al. (2015). Representation of microphysical processes in cloud-resolving models: Spectral (bin) microphysics versus bulk parameterization. *Reviews of Geophysics*, *53*, 247–322. https://doi.org/10.1002/2014RG000468

Lim, K.-S. S., & Hong, S.-Y. (2010). Development of an effective double-moment cloud microphysics scheme with prognostic cloud condensation nuclei (CCN) for weather and climate models. *Monthly Weather Review*, *138*(5), 1587–1612. https://doi.org/10.1175/2009MWR2968.1

McFarquhar, G. M., & Black, R. A. (2004). Observations of particle size and phase in tropical cyclones: Implications for mesoscale modeling of microphysical processes. *Journal of the Atmospheric Sciences*, *61*(4), 422–439. https://doi.org/10.1175/1520-0469(2004)061<0422:OOPSAP>2.0.CO;2

McFarquhar, G. M., Jewett, B. F., Gilmore, M. S., Nesbitt, S. W., & Hsieh, T.-L. (2012). Vertical velocity and microphysical distributions related to rapid intensification in a simulation of Hurricane Dennis (2005). *Journal of the Atmospheric Sciences*, *69*(12), 3515–3534. https://doi.org/10.1175/JAS-D-12-016.1

McFarquhar, G. M., Zhang, H., Heymsfield, G., Halverson, J. B., Hood, R., Dudhia, J., & Marks, F. Jr. (2006). Factors affecting the evolution of Hurricane Erin (2001) and the distributions of hydrometeors: Role of microphysical processes. *Journal of the Atmospheric Sciences*, *63*(1), 127–150. https://doi.org/10.1175/JAS3590.1

Morrison, H., Curry, J. A., & Khvorostyanov, V. I. (2005). A new double-moment microphysics parameterization for application in cloud and climate models. Part I: Description. *Journal of the Atmospheric Sciences*, *62*(6), 1665–1677. https://doi.org/10.1175/JAS3446.1

Park, H. S., Ryzhkov, A. V., Zrnić, D. S., & Kim, K.-E. (2009). The hydrometeor classification algorithm for the polarimetric WSR-88D: Description and application to an MCS. *Weather and Forecasting*, *24*(3), 730–748. https://doi.org/10.1175/2008WAF2222205.1

Pattnaik, S., Inglish, C., & Krishnamurti, T. N. (2010). Influence of rain-rate initialization, cloud microphysics, and cloud torques on hurricane intensity. *Monthly Weather Review*, *139*(2), 627–649. https://doi.org/10.1175/2010MWR3382.1

Pruppacher, H. R., & Klett, J. D. (2010). *Microphysics of clouds and precipitation*, (Vol. 18). Netherlands: Springer. https://doi.org/10.1007/978-0-306-48100-0

Putnam, B. J., Xue, M., Jung, Y., Zhang, G., & Kong, F. (2017). Simulation of polarimetric radar variables from 2013 CAPS spring experiment storm-scale ensemble forecasts and evaluation of microphysics schemes. *Monthly Weather Review*, *145*(1), 49–73. https://doi.org/10.1175/MWR-D-15-0415.1

Rogers, R. F., Black, M. L., Chen, S. S., & Black, R. A. (2007). An evaluation of microphysics fields from mesoscale model simulations of tropical cyclones. Part I: Comparisons with observations. *Journal of the Atmospheric Sciences*, *64*(6), 1811–1834. https://doi.org/10.1175/JAS3932.1

Skamarock, W. C., Klemp, J. B., Dudhia, J., Gill, D. O., Barker, D. M., Wang, W., & Powers, J. D. (2005). A description of the Advanced Research WRF Version 2, 88 pp.

Snyder, J. C., Bluestein, H. B., Dawson, D. T. II, & Jung, Y. (2017a). Simulations of polarimetric, X-band radar signatures in supercells. Part I: Description of experiment and simulated ρhv rings. *Journal of Applied Meteorology and Climatology*, *56*(7), 1977–1999. https://doi.org/10.1175/JAMC-D-16-0138.1

Snyder, J. C., Bluestein, H. B., Dawson, D. T. II, & Jung, Y. (2017b). Simulations of polarimetric, X-band radar signatures in supercells. Part II: ZDR columns and rings and KDP columns. *Journal of Applied Meteorology and Climatology*, *56*(7), 2001–2026. https://doi.org/10.1175/JAMC-D-16-0139.1

Steiner, M., Houze, R. A., & Yuter, S. E. (1995). Climatological characterization of three-dimensional storm structure from operational radar and rain gauge data. *Journal of Applied Meteorology*, *34*(9), 1978–2007. https://doi.org/10.1175/1520-0450(1995)034<1978:CCOTDS>2.0.CO;2

Tao, W.-K., Shi, J., Chen, S., Lang, S., Lin, P.-L., Hong, S.-Y., et al. (2011). The impact of microphysical schemes on hurricane intensity and track. *Asia-Pacific Journal of Atmospheric Sciences*, *47*(1), 1–16. https://doi.org/10.1007/s13143-011-1001-z

Thompson, G., & Eidhammer, T. (2014). A study of aerosol impacts on clouds and precipitation development in a large winter cyclone. *Journal of the Atmospheric Sciences*, *71*(10), 3636–3658. https://doi.org/10.1175/JAS-D-13-0305.1

Thompson, G., Field, P. R., Rasmussen, R. M., & Hall, W. D. (2008). Explicit forecasts of winter precipitation using an improved bulk microphysics scheme. Part II: Implementation of a new snow parameterization. *Monthly Weather Review*, *136*(12), 5095–5115. https://doi.org/10.1175/2008MWR2387.1

Tokay, A., Bashor, P. G., Habib, E., & Kasparis, T. (2008). Raindrop size distribution measurements in tropical cyclones. *Monthly Weather Review*, *136*(5), 1669–1685. https://doi.org/10.1175/2007MWR2122.1

Tong, M., & Xue, M. (2005). Ensemble Kalman filter assimilation of Doppler radar data with a compressible nonhydrostatic model: OSS experiments. *Monthly Weather Review*, *133*(7), 1789–1807. https://doi.org/10.1175/mwr2898.1

Vivekanandan, J., Adams, W. M., & Bringi, V. N. (1991). Rigorous approach to polarimetric radar modeling of hydrometeor orientation distributions. *Journal of Applied Meteorology*, *30*(8), 1053–1063. https://doi.org/10.1175/1520-0450(1991)030<1053:RATPRM>2.0.CO;2

Vivekanandan, J., Ellis, S. M., Oye, R., Zrnić, D. S., Ryzhkov, A. V., & Straka, J. (1999). Cloud microphysics retrieval using S-band dual-polarization radar measurements. *Bulletin of the American Meteorological Society*, *80*(3), 381–388. https://doi.org/10.1175/1520-0477 (1999)080<0381:CMRUSB>2.0.CO;2

Wang, M., Xue, M., & Zhao, K. (2016). The impact of T-TREC-retrieved wind and radial velocity data assimilation using EnKF and effects of assimilation window on the analysis and prediction of Typhoon Jangmi (2008). *Journal of Geophysical Research – Atmospheres*, *121*, 259–277. https://doi.org/10.1002/2015JD024001

Wang, M., Xue, M., Zhao, K., & Dong, J. (2014). Assimilation of T-TREC-retrieved winds from single-Doppler radar with an ensemble Kalman filter for the forecast of Typhoon Jangmi (2008). *Monthly Weather Review*, *142*(5), 1892–1907. https://doi.org/10.1175/MWR-D-13-00387.1

Wang, M., Zhao, K., Lee, W.-C., & Zhang, F. (2018). Microphysical and kinematic structure of convective-scale elements in the inner rainband of Typhoon Matmo (2014) after landfall. *Journal of Geophysical Research-Atmospheres*, *123*(12), 6549–6564. https://doi.org/10.1029/2018JD028578

Wang, M., Zhao, K., Xue, M., Zhang, G., Liu, S., Wen, L., & Chen, G. (2016). Precipitation microphysics characteristics of a Typhoon Matmo (2014) rainband after landfall over eastern China based on polarimetric radar observations. *Journal of Geophysical Research-Atmospheres*, *121*(20), 12415–12433. https://doi.org/10.1002/2016JD025307

Wen, L., Zhao, K., Chen, G., Wang, M., Zhou, B., Huang, H., et al. (2018). Drop size distribution characteristics of seven typhoons in China. *Journal of Geophysical Research-Atmospheres*, *123*(12), 6529–6548. https://doi.org/10.1029/2017JD027950

Whitaker, J. S., & Hamill, T. M. (2012). Evaluating methods to account for system errors in ensemble data assimilation. *Monthly Weather Review*, *140*(9), 3078–3089. https://doi.org/10.1175/mwr-d-11-00276.1

Yang, M.-J., & Ching, L. (2005). A modeling study of Typhoon Toraji (2001): Physical parameterization sensitivity and topographic effect. *Terrestrial, Atmospheric and Oceanic Sciences*, *16*(1), 177–213.

Zhang, G., Vivekanandan, J., & Brandes, E. (2001). A method for estimating rain rate and drop size distribution from polarimetric radar measurements. *IEEE Transactions on Geoscience and Remote Sensing*, *39*(4), 830–841. https://doi.org/10.1109/36.917906

Zhu, T., & Zhang, D.-L. (2006). Numerical simulation of Hurricane Bonnie (1998). Part II: Sensitivity to varying cloud microphysical processes. *Journal of the Atmospheric Sciences*, *63*(1), 109–126. https://doi.org/10.1175/JAS3599.1